Engineering with Computers
https://doi.org/10.1007/s00366-025-02154-8

ORIGINAL ARTICLE

Topology optimization with material point method: investigation into the design sensitivity and the effect of shape functions

Sanghyeon Park[1] · **Byeonghyeon Goh**[1] · **Hayoung Chung**[1]

Received: 25 November 2024 / Accepted: 18 April 2025

Abstract
The Material Point Method (MPM) is considered promising for analyzing structures that experience large displacements and extreme events, areas where typical mesh-based analysis methods falter due to mesh distortion. By leveraging both Eulerian and Lagrangian descriptions, MPM facilitates the easy application of boundary conditions, overcoming the inherent limitations of mesh-based approaches. However, integrating MPM into topology optimization has been hindered by challenges in deriving analytical sensitivities and inherent numerical inaccuracies. This study introduces a novel topology optimization approach that employs MPM instead of the finite element method. The design variable is parameterized by material point volumes that utilize point-wise properties to represent design layouts. This approach addresses the calculation and validation of analytical design sensitivities and significantly enhances design flexibility, as the density of the design variable is not confined to an existing grid and can be user-defined. Furthermore, the research explores the effects of cell crossing errors on the stress field within topology optimization and proposes modifications to the shape function to mitigate these errors, thereby improving the applicability of MPM.

Keywords Topology optimization · Material point method · Meshfree method · Quasistatic implicit formulation · Cell crossing error

1 Introduction

Topology optimization is a mathematical method that is used to determine the optimal distribution of materials within a design, aiming to minimize a specific objective while adhering to predefined constraints. This technique is particularly beneficial for creating lightweight structures that offer a high degree of design freedom and is widely applied in various engineering disciplines, including the aerospace [1] and automotive [2] fields. Traditionally, the finite element method (FEM) is utilized to analyze structural responses and to derive sensitivities for both optimal and intermediate design outcomes. However, relying on mesh-based discretization introduces several challenges. These include difficulties in achieving accurate results under severe structural nonlinearities, such as during contact, impact [3], or when faced with issues such as mesh distortion [4] and material fragmentation [5, 6]. Furthermore, when mesh-based variables are employed as design variables, typically seen in the solid isotropic material penalization (SIMP) method, the flexibility of the design variable, particularly with regard to resolution, becomes constrained. Enhancing the resolution beyond the mesh's limits or adjusting the design domain's granularity typically necessitates complex numerical interventions, such as remeshing [7] and employing multi-resolution topology optimization [8–10].

In response to these challenges, extensive research has been conducted on meshfree methods as viable alternatives to FEM in topology optimization. Two primary approaches have been developed for applying meshfree methods in this field. The first approach is where meshless methods are employed solely to facilitate the representation of design variables: Neofytou et al. [11] employed the reproduced kernel particle method (RKPM) to adaptively add boundary

S. Park contributed to the Methodology, Software, Writing, Revising. B. Goh contributed to the Methodology, Software. H. Chung contributed to the Conceptualization, Methodology, Writing, Revising, Funding Acquisition and is the corresponding author.

✉ Hayoung Chung
hychung@unist.ac.kr

[1] Department of Mechanical Engineering, Ulsan National Institute of Science and Technology, 50 UNIST-gil, Ulju-gun, Ulsan 44919, South Korea

Published online: 07 May 2025

nodes, while Wang et al. [12] used the radial point interpolation method (RPIM) to optimize microstructural composite design. This method integrates the design variables with the homogenization technique to determine the effective properties of the composites and enable their inverse design. The second approach replaces FEM with meshless methods for structural analysis, including Conner et al. [13] and Masoero et al. [14] where the discrete element method is incorporated into density-based topology optimization. Meanwhile, RKPM [15] and other meshfree methods have also shown considerable promise in a variety of topology optimization [16–19].

However, replacing FEM with meshfree methods introduces several numerical challenges that require careful consideration. As pointed out by Garg et al. [20], meshfree methods typically offer lower numerical accuracy and efficiency compared to FEM. Moreover, applying boundary conditions with meshfree methods is notably more complex, a crucial aspect since the accuracy of analysis is essential for effective topology optimization, as emphasized by Krongauz et al. [21].

Therefore, Sulsky et al. [22] first introduced the material point method (MPM), which effectively integrates the advantages of both Lagrangian and Eulerian descriptions. The MPM utilizes an Eulerian background grid to solve the governing equations and to facilitate interactions among Lagrangian material points, thus significantly reducing mesh distortion [23, 24]. This method offers enhanced convenience for imposing boundary conditions and external forces compared to traditional Lagrangian or Eulerian approaches [25]. Furthermore, MPM is particularly adept at providing precise simulations of large deformations and complex materials behavior, demonstrating substantial improvements over conventional methods in these areas [23, 26, 27].

The MPM has been utilized in the field of topology optimization, significantly advancing the capabilities of structural analysis and design. As a hybrid Lagrangian–Eulerian method, MPM combines the advantages of both descriptions, allowing it to effectively handle large deformations and prevent mesh distortion. These features make MPM particularly suitable for problems involving extreme deformations, contact interactions, and mesh distortion, where mesh-based methods may encounter difficulties. Li et al. [28] first proposed the use of a material point as an analysis step in topology optimization. Similar studies have been conducted using Taichi [29], an open-source programming language designed for high performance numerical computations with MPM. Recent advances by researchers such as Yuhn et al. [30] and Sato et al. [31] have leveraged Taichi MPM to introduce methodologies for time-varying density-based topology optimization. These studies focus on optimizing both the structural configuration and the dynamic movement of the body simultaneously by demonstrating the advantages of MPM in topology optimization, particularly in extreme events such as large deformation and contact scenario. However, to the best knowledge of the authors, there is no existing literature on sensitivity analysis and the effect of cell crossing error on topology optimization. Sensitivity analysis is crucial as it assess how variations in optimization parameters affect the objective function, thereby validating and ensuring the robustness of topology optimization outcomes [32]. Cell crossing error, a well-known issue in MPM, occurs whenever material points move across grid boundaries, which can lead to inaccurate structural analysis. Therefore, addressing cell crossing error is essential to ensure the accurate performance of topology optimization.

In this work, we introduce a novel density-based topology optimization technique utilizing the implicit quasistatic MPM under linear elastic strain. Here, the material point itself serves as the design variable. Analytical sensitivity is derived and validated through comparison with numerical sensitivity, addressing both self-adjoint and non-self-adjoint issues that arise from the use of derived analytical sensitivities. Additionally, this study focuses on on the impact of cell crossing errors on topology optimization and proposes methods to mitigate these effects. Furthermore, we demonstrate the capability of multi-resolution topology optimization, capitalizing on the ability to separate material points from the background grid. This separation facilitates multi-resolution topology optimization with varying distributions of material points.

The structure of this paper is organized as follows: Sect. 2 provides a detailed overview of the implicit quasistatic MPM method employed in this study. Specifically, this section includes the governing equation and shape functions. Based on the MPM presented, Sect. 3 describes the optimization approach that integrates MPM into topology optimization. This section includes the optimization problem, where two types of objectives are addressed: compliance and stress minimization. The section elucidates how MPM works to achieve optimal designs and highlights its validity and effectiveness in the optimization process. Accordingly, Sect. 4 presents the design sensitivities related to material points that are calculated using an adjoint method. Section 5 provides numerical examples in cases with and without cell crossing error, thus investigating the impact of the error on the optimization results. Section 6 presents the additional benefits of the proposed method using MPM. Finally, Sect. 7 concludes and summarizes the findings and contributions of this research.

2 Material point method

The MPM is a Lagrangian particle method developed as an extension of the fluid implicit particle method [22], designed to address challenges in continuum solid mechanics. The

primary advantages of MPM stem from its unique integration of both Lagrangian and Eulerian descriptions, which facilitates a comprehensive approach to modeling solids. This method effectively resolves mesh-related issues such as mesh distortion and element entanglement. Additionally, MPM is seamlessly compatible with the FEM, due to its utilization of weak-form formulations, enhancing its applicability across different computational mechanics.

Figure 1 illustrates the domain representation typically employed in MPM, where the continuum body Ω is represented by a number of Lagrangian material points positioned on the Eulerian fixed grid E. The continuum variables, such as stress and displacement, are evaluated at the material points at their respective material coordinates (i.e., $\boldsymbol{x}$ in Ω). It is customary to associate a material point with a quadrature point in FEM. It is worth noting that the number of material points within a grid cell can vary depending on the required accuracy [33–35].

In this work, implicit quasistatic MPM [36] was utilized, as it provides numerous advantages, such as the ability to accommodate complex constitutive models [37], capture large time-scale responses [38–40], and increase numerical stability [36], which are crucial for stress analysis [41], which is essential to solve static problems considered in the present work. In this section, we provide a brief description of the governing equation for the implicit quasistatic MPM. Detailed formulations are available in the study by Charlton et al. [36].

2.1 Governing equation

At static equilibrium, the governing equation for the structure is given by:

$$\int_{\Omega} (\boldsymbol{\sigma} : \delta \nabla \boldsymbol{u})\, dV - \int_{\Omega} (\eta \boldsymbol{b} \cdot \delta \boldsymbol{u})\, dV - \int_{\partial\Omega} (\boldsymbol{t} \cdot \delta \boldsymbol{u})\, dA = 0, \tag{1}$$

where Ω is the volume of the structure, and η is the specific density. Further, $\boldsymbol{u}$ and $\delta\boldsymbol{u}$ represent the displacement and the virtual displacement, respectively. The Cauchy stress within the body is indicated by $\boldsymbol{\sigma}$, which is induced by external loads, including the specific body force $\boldsymbol{b}$ and the boundary traction $\boldsymbol{t}$ applied on the boundary $\partial\Omega$. Equation 1 is equivalent to the updated Lagrangian formulation of a continuum body [3].

In MPM, the displacement of the material point $\boldsymbol{u}$ is approximated by the displacement of background grid $\boldsymbol{d}_I$:

$$\boldsymbol{u} = \sum_{I=1}^{N_n} (S_{vp})_I \boldsymbol{d}_I \tag{2}$$

where S_{vp} is the shape function that facilitates the interaction between the Lagrangian material points and the Eulerian background grid, I is the Eulerian background grid index, and N_n is the number of nodes. The equilibrium equation over the background grid is:

$$\begin{aligned} &\int_E \left([\nabla_x S_{vp}]^{\mathrm{T}} \boldsymbol{\sigma} : \delta \boldsymbol{u}\right) dV - \int_E \left([S_{vp}]^{\mathrm{T}} \eta \boldsymbol{b} \cdot \delta \boldsymbol{u}\right) dV \\ &- \int_{\partial E} \left([S_{vp}]^{\mathrm{T}} \boldsymbol{t} \cdot \delta \boldsymbol{u}\right) dA = 0. \end{aligned} \tag{3}$$

where $\delta\boldsymbol{u}$ denotes the virtual nodal displacement. The first integral term in Eq. (3) represents the internal virtual work within a grid cell, while the second and third terms represent the external virtual work due to the body and traction forces, respectively. Following [42], volume integration is approximated by numerical integration, where material points are considered as quadrature points. The body force term in Eq. (3) is assumed to be negligible, and the traction force term is calculated as a mapping from the surface to the body. In the implicit MPM, the physical domain is discretized into material points, which are employed to numerically compute the stiffness of background grid cells as calculated in Eq. (2). Consequently, Eq. (3) leads to the internal force ($\boldsymbol{f}_E^{\mathrm{int}}$) and the external force ($\boldsymbol{f}_E^{\mathrm{ext}}$) defined on the grid as follows:

$$\begin{aligned} &\sum_{N=1}^{N_{mp}} \delta \boldsymbol{d}_N^{\mathrm{T}} \left([\nabla_x S_{vp}]_N^{\mathrm{T}} \cdot \boldsymbol{\sigma} \cdot (V_p)_N\right) - \sum_{N=1}^{N_{mp}} \delta \boldsymbol{d}_N^{\mathrm{T}} \left([S_{vp}]_N^{\mathrm{T}} (\boldsymbol{f}_p^{\mathrm{ext}})_N\right) \\ &= \delta \boldsymbol{d}_N^{\mathrm{T}} \left(\boldsymbol{f}_E^{\mathrm{int}} - \boldsymbol{f}_E^{\mathrm{ext}}\right) = \delta \boldsymbol{d}_N^{\mathrm{T}} \cdot \boldsymbol{R} = \boldsymbol{0}. \end{aligned} \tag{4}$$

where N_{mp} denotes the number of material points, V_p represents the volume of the material point, and $\boldsymbol{f}_p^{\mathrm{ext}}$ is the external force at the material point. $\boldsymbol{R}$ is the residual force vector, and a standard Newton iteration method is used to calculate the equilibrium, i.e. $\boldsymbol{R} = 0$, with a tolerance of $|\boldsymbol{R}| \leq 10^{-9}$. Linearizing $\boldsymbol{f}_E^{\mathrm{int}}$, one can obtain the stiffness of the grid element $\boldsymbol{K}_E$ and the material point $\boldsymbol{K}_p$:

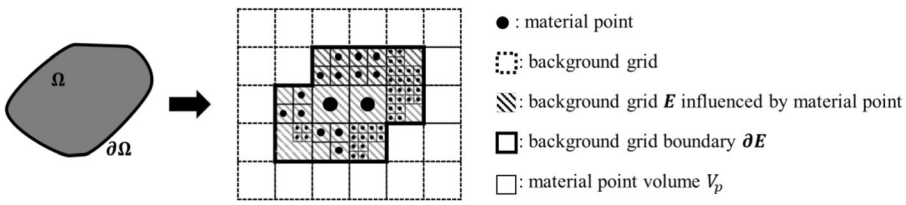

Fig. 1 Schematics of the material point method (MPM)

$$\begin{aligned}\left[\boldsymbol{k}_E\right] &= \int_E \left[\nabla_x S_{vp}\right]^{\mathrm{T}} [\boldsymbol{\alpha}] \left[\nabla_x S_{vp}\right] dV \\ &\cong \sum \left[\boldsymbol{K}_p\right], \text{where } [\boldsymbol{\alpha}] = \boldsymbol{D} \\ &= \frac{E}{(1+\nu)(1-2\nu)} \begin{pmatrix} 1-\nu & \nu & 0 \\ \nu & 1-\nu & 0 \\ 0 & 0 & \frac{1-2\nu}{2} \end{pmatrix}\end{aligned} \tag{5}$$

where $\boldsymbol{\alpha}$ is the spatial consistent tangent modulus [36] for a material point within the background grid cell. As linear elastic material is used in this study, the spatially consistent tangent modulus is equal to the isotropic material stiffness tensor $\boldsymbol{D}$ with Young's modulus E and Poisson's ratio ν.

2.2 Shape functions

In the MPM, material behavior is largely determined by the shape function S_{vp}, which facilitates the projection of physical quantities-including mass, momentum, and internal forces-between material points and background grid nodes. Accordingly, the continuity of the shape function is crucial to the accuracy and stability of the method. If continuity is compromised, the accuracy of the solution can immensely deteriorate. If continuity is compromised, the accuracy of the solution can immensely deteriorate. For instance, the stress field becomes fictitiously discontinuous when the material points traverse the background grid cells, and the grid-material point pairs change abruptly. In particular, the standard MPM [22] faces challenges in integrating internal forces (Eq. (4)) and computing the stiffness matrix (Eq. (5)), primarily due to the discontinuity of the gradients of the shape function. This parasitic phenomenon, often referred to as the cell crossing error [43–45], is widely known, and several numerical remedies have been proposed to mitigate the error. One of the early efforts to reduce the error includes the development of the generalized interpolation material point (GIMP) method by Bardenhagen and Kober [46], where each material point possesses its domain, and the associated shape function, S_{vp}^G, is smoother than the standard shape function S_{vp}^0 [22]. The standard shape function S_{vp}^0 and the generalized interpolation function S_{vp}^G are as follows:

$$S_{vp}^0 = \begin{cases} 1 + (\tilde{X}_p - \tilde{X}_v)/h & -h < \tilde{X}_p - \tilde{X}_v \le 0 \\ 1 - (\tilde{X}_p - \tilde{X}_v)/h & 0 < \tilde{X}_p - \tilde{X}_v \le h \end{cases} \tag{6}$$

$$S_{vp}^G = \begin{cases} (h + l_p + \tilde{X}_p - \tilde{X}_v)^2/4hl_p & -h - l_p < \tilde{X}_p - \tilde{X}_v \le -h + l_p \\ 1 + (\tilde{X}_p - \tilde{X}_v)/h & -h + l_p < \tilde{X}_p - \tilde{X}_v \le -l_p \\ 1 - (\tilde{X}_p - \tilde{X}_v)^2/2hl_p & -l_p < \tilde{X}_p - \tilde{X}_v \le l_p \\ 1 - (\tilde{X}_p - \tilde{X}_v)/h & l_p < \tilde{X}_p - \tilde{X}_v \le h - l_p \\ (h + l_p - \tilde{X}_p + \tilde{X}_v)^2/4hl_p & h - l_p < \tilde{X}_p - \tilde{X}_v \le h + l_p \end{cases} \tag{7}$$

where h represents the size of the background grid cell, $\tilde{X}_p$ and $\tilde{X}_v$ denote the positions of the material point and the background grid, respectively. $l_{p,x}$ and $l_{p,y}$ are half the horizontal and vertical lengths of the material point domain, as shown in Fig. 2.

Note that the gradient of the standard interpolation function S_{vp}^0 is discontinuous at the regions denoted 1, 2, and 3, while S_{vp}^G is not, as shown in Figs. 2 (a) and (b). The difference between the two interpolation functions can also be seen in their effect on the grid cells of the material point. Figure 2 (b) shows that not only is the cell containing the material point affected, but also the cells that overlap with the material point domain. Consequently, more rectangular red boxes representing background grids affected by the material point are involved in the analysis in the GIMP method, as shown in Figs. 2 (a) and (b).

In this work, we thoroughly investigated for the first time the effects of using different shape functions on topology optimization. Our focus was particularly on enhancing the accuracy of both structural and sensitivity analyses in the presence of cell crossing error, which ultimately influences the outcomes of topology optimization.

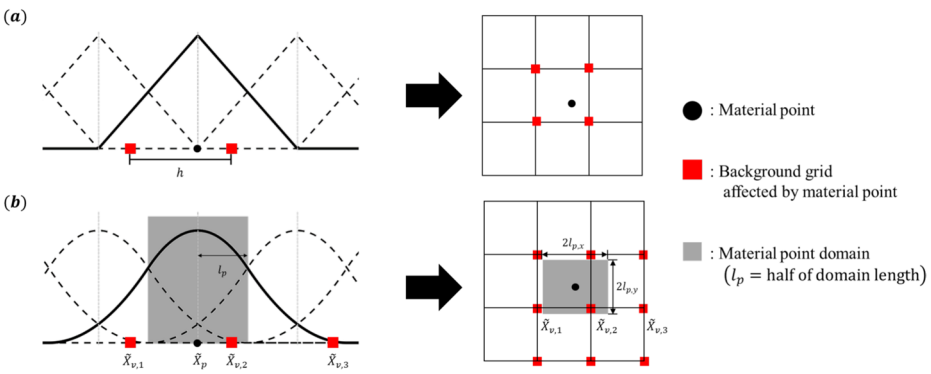

Fig. 2 Material point interpolation function: (a) standard interpolation (S_{vp}^0) and (b) generalized interpolation (S_{vp}^G) in one dimension

3 Topology optimization

This section presents the proposed topology optimization. The problem definition is first presented, which is followed by in-depth research regarding the feasibility of using V_p as a design variable, and the formulation of the sensitivity of the objective function with respect to the terms of the material point and the background grid.

3.1 Optimization problem

The problem is formulated to minimize either of the objectives — compliance J_1 or stress objective J_2 — subject to a specified volume constraint V^*, which serves as an upper bound on the volume $V(\rho)$ occupied within the design domain E:

$$\begin{aligned} \min_{\boldsymbol{\rho}} \quad & J_1(\boldsymbol{\rho}) = c(\boldsymbol{\rho}) = \left(\boldsymbol{f}_{\text{ext}}^T \cdot \boldsymbol{u}\right)_p, \quad J_2(\boldsymbol{\rho}) = \boldsymbol{\sigma}_{PN}(\boldsymbol{\rho}) \\ \text{Subject to:} \quad & \boldsymbol{R} = \boldsymbol{f}_p^{\text{int}} - \boldsymbol{f}_p^{\text{ext}} = 0, \\ & V(\boldsymbol{\rho}) \le V^*, \\ & 0 < \boldsymbol{\rho}_{\min} \le \boldsymbol{\rho} \le 1, \end{aligned} \tag{8}$$

where $\boldsymbol{\rho}$ is the density of the material point, serving as the design variable. The p-norm stress aggregation scheme is utilized to compute the stress objective function $\boldsymbol{\sigma}_{PN}$ as outlined in [47]:

$$\begin{aligned} \boldsymbol{\sigma}_{PN}(\boldsymbol{\rho}) &= \left(\sum_{mp=1}^{N_{mp}} \hat{\boldsymbol{\sigma}}_{vm,mp}^{p}\left(\boldsymbol{\rho}_{mp}\right) \right)^{1/p} \\ &= \left(\sum_{mp=1}^{N_{mp}} \rho_{mp}^{q} \boldsymbol{\sigma}_{vm,mp}^{p}\left(\boldsymbol{\rho}_{mp}\right) \right)^{1/p} \end{aligned} \tag{9}$$

where $\boldsymbol{\sigma}_{vm,mp}^{p}$ is the von-Mises stress calculated at mp-th material point. The parameters p and q are used in the p-norm aggregation scheme [48, 49], and represent the general stress penalization parameter [48, 50, 51], respectively. Although stress minimization is less common than imposing stress constraints, problem definition Eq. (8) is maintained for consistency throughout the paper. $\boldsymbol{R}$ is the residual regarding the static equilibrium of the structure. It is worth noting that the equilibrium equation Eq. (4) is stated in terms of material points, and the forces are projected from those on the grid.

3.2 Design variable

As previously mentioned, this study employs the density assigned to material points as a design variable. Specifically, the point-wise design variable $\boldsymbol{\rho}$ is calculated as a scaled volume V_p/V_p^0, where V_p^0 denotes the domain volume and V_p is the material volume.

It is noteworthy that the design variable $\boldsymbol{\rho}(x)$ represents the amount of material at the point x, the initial location of the corresponding material point, as is typical in density-based topology optimization methods. This variable assumes a continuous scalar value ranging from 0 to 1 due to scaling. Consequently, Young's modulus assigned to the material point E_p is calculated similarly to the approach used in the SIMP method:

$$E_p(\boldsymbol{\rho}) = E_{\min} + \boldsymbol{\rho}^{pl}\left(E_0 - E_{\min}\right), \tag{10}$$

Here, pl represents the penalization factor, and E_0 is the Young's modulus of the material. To avoid numerical singularity, a fictitiously small Young's modulus, $E_{\min}$, is introduced, and its value is 10^{-6}. Although this method is the simplest among other design parameterization techniques that utilize particle-wise variables, it offers significant advantages. It is not only readily differentiable (i.e., it does not require additional constraints [30]) and is inherently binary, but it also integrates seamlessly into the typical topology optimization pipeline, such as the SIMP method.

However, it is important to note that using V_p to represent the design raises a critical question about the equivalence of removing a material point with a localized zero material density, especially since numerical integration and the grid-to-point (G2P) and point-to-grid (P2G) mapping processes differ in these scenarios. This question is also crucial as it pertains to the flexibility of the design representation, which comes from the fact that V_p^0 is variable and can change depending on the number of material points. To address this issue, we examine the impact of localized near-zero material density on the structural response in this section. Figure 3 illustrates the three models with the same problem domain but different number of material points to represent the same toy cantilever model, with a tip load $\boldsymbol{F}$. One-sixteenth of the upper top material is assumed to be removed. This removal is modeled in three different ways: by eliminating a single material point (Fig. 3 (a)), by assigning zero material density to a particle where $V_p^0 = 1/4$ (Fig. 3 (b)), and by distributing the removal across four particles, each with $V_p^0 = 1/16$ (Fig. 3 (c)). For brevity, the former and latter cases hereafter are referred to as case 1, 2, and 3, respectively:

The magnitude of nodal displacements ($|\boldsymbol{d_I}|$) for the material indexed in Fig. 3 (a), analyzed using the MPM and interpolated, is presented in Fig. 4. It is clearly observed that the displacements of the background grid in case 1 and case 2 are identical, demonstrating that a zero-density material point is equivalent to the absence of a material with the same volume fraction. This equivalence persists even when V_p^0 is reduced by a quarter, as shown in Fig. 3 (c), where

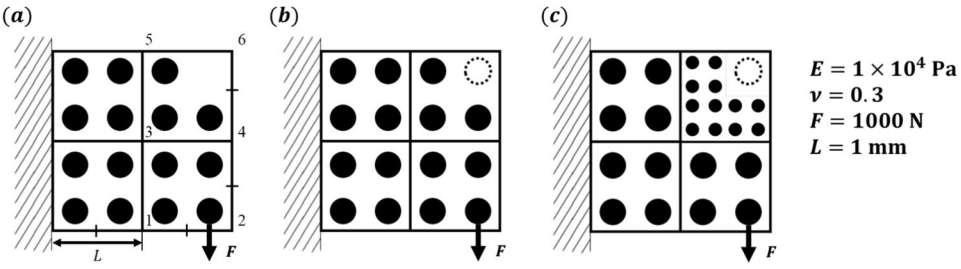

Fig. 3 Material point distribution in a background grid with force applied to one material point: (a) case 1: The top-right corner material point is removed; (b) case 2: The top-right corner material point has zero density; (c) case 3: Three material points are replaced by twelve material points in case 2

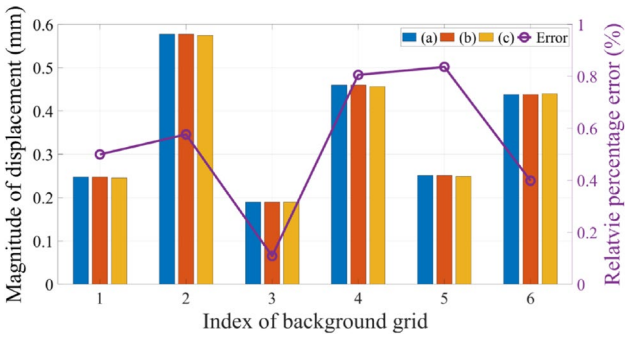

Fig. 4 The magnitude of nodal displacements ($|\boldsymbol{d_I}|$) for the material indexed in Fig. 3 (a) and its relative percentage error between the case 2 case 3

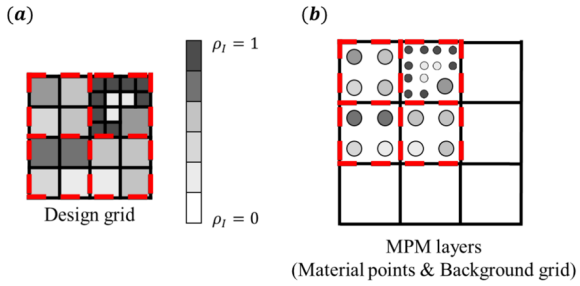

Fig. 5 Configuration of **a** the design grid and **b** MPM layers, where the material points are situated on a background grid. The size of the design grid (indicated by a red dashed line) matches the size of the background grid cell that houses the initial-state material point

the design resolution is accordingly refined. Although the magnitudes $|\boldsymbol{d_I}|$ do not exactly match those in the previous cases, all errors are smaller than 1.0% and do not vary with the location of node I, as illustrated in Fig. 4.

3.3 Implementation of the algorithm

This section outlines the proposed topology optimization method and its accompanying algorithm, both of which are crucial for implementation. In this method, the design variable ρ is stored on a separate design grid, distinct from the MPM layers (i.e., the material points and the background grid). This separation is necessary because the background Cartesian grid is much larger than the structural domain, as it needs to fully encompass the material points within the Eulerian grid. Additionally, updating the design variables during optimization can be cumbersome if ρ is defined as a member variable of a material point, since it is typically implemented as an individual object and does not communicate within each optimization iteration. As described in Section 3.2, the only constraints for storing design variables are the dimensions of these variables and the undeformed coordinate of the material points. Consequently, a simple adaptive Cartesian grid is employed in this study, as depicted in Fig. 5.

As shown in Fig. 5 (a), the design grid, a structured Cartesian grid with quadtree refinement, stores the density ρ_I of the particles labeled I. The centroid of each element corresponds to the initial location of its material point, and the element size is proportional to V_p^0. The introduction of a design grid, akin to those found in density-based methods, facilitates the incorporation of widely used numerical techniques such as filtering [52], erosion-dilatation [53], and manufacturing constraints [54].

A flowchart of the algorithm is shown in Fig. 6. Once the optimization problem and design domain are defined, material points are generated within the background grid. The initial material volume V_p^0 and the width of the shape function h are determined accordingly, leading to the creation of a design grid based on these parameters. As mentioned earlier, the design variable ρ on this grid is similar to the density field in the SIMP method; therefore, we employ several numerical techniques such as filtering [55] and penalization [56] on the design variables. Initially, ρ is set based on the volume constraint. The density in the design grid is then mapped onto the material points, where the total of material volume V_p is computed. Structural analysis is conducted using the MPM, during which the point-wise variables specified in Eqs. (4) and (5) are calculated. These variables are subsequently used in sensitivity analysis. The design variables are updated based on the increment $\Delta\rho$ that is obtained through the gradient-based optimization, considering both the objective functions and constraints and their sensitivities. The iterative process continues until the stopping criterion is met, which in this case is defined by a deviation between the

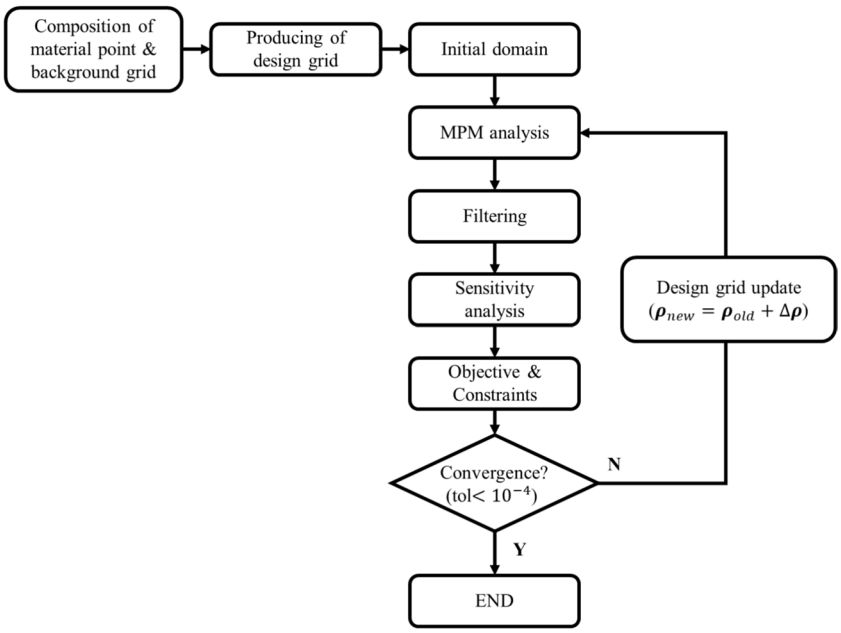

Fig. 6 Flowchart of topology optimization using the MPM

current objective value and that of the previous four iterations falling within a tolerance of 10^{-4}.

4 Sensitivity analysis

In this section, we present the analytical sensitivity of the objective function, based on the adjoint method. The Lagrangian functional $\mathcal{L}$ can be written as:

$$\mathcal{L}(\boldsymbol{\rho}, \boldsymbol{u}) = J(\boldsymbol{\rho}, \boldsymbol{u}) + \lambda^{\mathrm{T}} \boldsymbol{R}(\boldsymbol{\rho}, \boldsymbol{u}), \tag{11}$$

where λ is the adjoint variable. From the definition of residual $\boldsymbol{R}$ in Eq. (8), the sensitivity of the augmented functional can be formulated as

$$\frac{d\mathcal{L}}{d\boldsymbol{\rho}} = \frac{\partial J}{\partial \boldsymbol{\rho}} + \frac{\partial J}{\partial \boldsymbol{u}_p} \cdot \frac{\partial \boldsymbol{u}_p}{\partial \boldsymbol{\rho}} + \lambda_p^T \left(\frac{\partial \boldsymbol{R}}{\partial \rho} + \frac{\partial \boldsymbol{R}}{\partial \boldsymbol{u}_p} \cdot \frac{\partial \boldsymbol{u}_p}{\partial \boldsymbol{\rho}} \right) \tag{12}$$

For simplicity, the external load $\boldsymbol{f}^{\mathrm{ext}}$, such as the body force and the deformation of the load (i.e., dead load), can be ignored without loss of generality, leading to the adjoint equation.

$$\begin{aligned} \lambda_p^T &= -\frac{\partial J}{\partial \boldsymbol{u}_p} \cdot \left(\frac{\partial \boldsymbol{f}_p^{\mathrm{int}}}{\partial \boldsymbol{u}_p} \right)^{-1} = -\left(\frac{\partial J}{\partial \boldsymbol{u}} \cdot \boldsymbol{K}^{-1} \right)_E \cdot \\ \left[S_{vp} \right] &= -\left(\frac{\partial J}{\partial \boldsymbol{u}} \cdot \boldsymbol{K}^{-1} \right)_p \end{aligned} \tag{13}$$

Note that λ, $\partial J / \partial \boldsymbol{u}_p$, and $\partial \boldsymbol{f}^{\mathrm{int}} / \partial \boldsymbol{u}_p$ are point-wise variables, as defined by Eq. (8). In the conventional FEA-based SIMP method, sensitivity analysis is performed using a fixed global stiffness matrix $\boldsymbol{K}$, which allows direct differentiation. However, in the implicit MPM used in this study, due to the Lagrangian material points, the computation of λ requires matrix inversion at each material point, leading to significant computational overhead. To alleviate this, we calculate these variables on the background grid using the global stiffness matrix $\boldsymbol{K}$ on the fixed grid E, similar to the FEA framework. Since design variables are associated with material points, but analysis is conducted on the background grid, the adjoint variable computed on the grid must be mapped back to material points. These processes are performed via the G2P operation, ensuring consistency while reducing computational costs. This ensures consistency between the design and analysis domains while accounting for the discretization approach of implicit MPM.

As a consequence, the design sensitivity of the objective function J with respect to the design variable ρ is simplified to:

$$\frac{d\mathcal{L}}{d\boldsymbol{\rho}} = \frac{\partial J}{\partial \boldsymbol{\rho}} - \left(\frac{\partial J}{\partial \boldsymbol{u}} \boldsymbol{K}^{-1} \right)_p \cdot \frac{\partial \boldsymbol{f}_p^{\mathrm{int}}}{\partial \boldsymbol{\rho}} \tag{14}$$

In this study, we focus on two objective functions: mechanical compliance J_1 and p-norm stress J_2, as shown in Eq. (8). The subsequent sections describe the derivation process, which is complex due to the duality of the variables present both at the material points and on the background grid. We also verify their design sensitivities (i.e., $dJ/d\rho$) as detailed in Appendix A, where they are compared to numerical differentiation methods.

4.1 Mechanical compliance

Being a self-adjoint, mechanical compliance (J_1) minimization problem concerns the adjoint variable equivalent to the displacement field $\boldsymbol{u}_p$ by assuming linear elasticity:

$$\begin{aligned}\lambda_p^T &= -\left(\frac{\partial J_1}{\partial \boldsymbol{u}} \cdot \boldsymbol{K}^{-1}\right)_p = \left(\frac{\partial \boldsymbol{f}_{\text{ext}}^T \cdot \boldsymbol{u}}{\partial \boldsymbol{u}} \cdot \boldsymbol{K}^{-1}\right)_p \\ &= \left(\boldsymbol{f}_{\text{ext}}^T \cdot \boldsymbol{K}^{-1}\right)_p = -\boldsymbol{u}_p^T.\end{aligned} \tag{15}$$

Note that this self-adjoint characteristic is valid as this work considers infinitesimally small deformations and linear elasticity; otherwise, the adjoint equation must be solved separately. Accordingly, the sensitivity becomes

$$\begin{aligned}\frac{dJ_1}{d\boldsymbol{\rho}} &= -\boldsymbol{u}_p^T \cdot \frac{\partial \boldsymbol{f}_p^{\text{int}}}{\partial \boldsymbol{\rho}} = -\boldsymbol{u}_p^T \cdot \frac{\partial \boldsymbol{K}_p}{\partial \boldsymbol{\rho}} \cdot \boldsymbol{u}_p. \\ &= -pl \cdot \boldsymbol{\rho}^{(pl-1)} \cdot \boldsymbol{u}_p^{\mathrm{T}} \cdot \boldsymbol{K}_p^0 \cdot \boldsymbol{u}_p.\end{aligned} \tag{16}$$

where $\boldsymbol{K}_p$ is the linearized contribution of the particle displacement to the internal force (i.e., particle stiffness) found in Eq. (5), and $\boldsymbol{K}_p^0$ denotes the stiffness when $\boldsymbol{\rho} = 1.0$.

4.2 P-norm stress

Given that p-norm stress is employed as the objective function, it is essential to calculate the sensitivity accurately, adhering to the characteristics of the p-norm. The design sensitivity of the p-norm can be articulated as follows:

$$\frac{dJ_2}{d\boldsymbol{\rho}} = \frac{\partial J_2}{\partial \boldsymbol{\rho}} - \lambda_p^{\mathrm{T}} \cdot \frac{\partial \boldsymbol{K}_p}{\partial \boldsymbol{\rho}} \cdot \boldsymbol{u}_p. \tag{17}$$

Based on the definition of p-norm stress in Eq. (9), the first term of Eq.(17) can be expressed as:

$$\frac{\partial J_2}{\partial \boldsymbol{\rho}} = \sum_{N=1}^{N_{mp}} \frac{\partial J_2}{\partial \hat{\sigma}_{vm,N}} \left[\left(\frac{\partial \hat{\sigma}_{vm,N}}{\partial \hat{\boldsymbol{\sigma}}_N}\right)^{\mathrm{T}} \frac{\partial \hat{\boldsymbol{\sigma}}_N}{\partial \boldsymbol{\rho}}\right], \tag{18}$$

where $\hat{\sigma}_N$ denotes the penalized stress measure shown in Eq. (9). The calculation of the second term in Eq. (17) is done with non-self-adjoint. This computation involves relating stress calculations to the grid and then mapping them to the particle, akin to the procedure in Eq. (13). Therefore, the adjoint variable for each material point in the p-norm stress minimization problem can be calculated as follows:

$$\begin{aligned}\lambda_p^T &= \left(\frac{\partial J_2}{\partial \boldsymbol{u}} \cdot \boldsymbol{K}^{-1}\right)_p \\ &= \left(\left(\sum_{N=1}^{N_{mp}} \frac{\partial J_2}{\partial \hat{\sigma}_{vm,N}} \left(\frac{\partial \hat{\sigma}_{vm,N}}{\partial \hat{\boldsymbol{\sigma}}_N}\right)^{\mathrm{T}} \boldsymbol{\rho}_N^q \cdot [\boldsymbol{\alpha}] \cdot \left[S_{vp}\right]_N\right) \boldsymbol{K}^{-1}\right)_p.\end{aligned} \tag{19}$$

Consequently, the p-norm stress sensitivity with respect to the design variable can be expressed as:

$$\begin{aligned}\frac{dJ_2}{d\boldsymbol{\rho}} &= \frac{\partial J_2}{\partial \boldsymbol{\rho}} - \lambda_p^{\mathrm{T}} \cdot \frac{\partial \boldsymbol{K}_p}{\partial \boldsymbol{\rho}} \cdot \boldsymbol{u}_p \\ &= \sum_{N=1}^{N_{mp}} \left[\frac{\partial J_2}{\partial \hat{\sigma}_{vm,N}} \left(\frac{\partial \hat{\sigma}_{vm,N}}{\partial \hat{\boldsymbol{\sigma}}_N}\right)^{\mathrm{T}} \frac{\partial \hat{\boldsymbol{\sigma}}_N}{\partial \boldsymbol{\rho}}\right] - pl \cdot \boldsymbol{\rho}^{(pl-1)} \\ &\quad \sum_{N=1}^{N_{mp}} \left\{\frac{\partial J_2}{\partial \hat{\sigma}_{vm,N}} \left(\frac{\partial \hat{\sigma}_{vm,N}}{\partial \hat{\boldsymbol{\sigma}}_N}\right)^{\mathrm{T}} \cdot \boldsymbol{\rho}_N^q \cdot [\boldsymbol{\alpha}] \cdot \left[S_{vp}\right]_N\right\} \cdot \boldsymbol{u}_p.\end{aligned} \tag{20}$$

This formulation clearly demonstrates the relation between the stress distribution and the design variables, affirming the critical role of an accurate stress calculation in obtaining optimal designs.

5 Benchmark problems

In this section, we consider well-understood topology optimization problems focusing on compliance and stress minimization, which serve to verify the accuracy of the design sensitivity and the validity of the optimized layouts. Additionally, these examples are tailored to elucidate the effects of the shape functions — namely, the standard MPM and the GIMP method — on the optimization process and the resulting optimized layouts.

Throughout this study, both the cantilever beam [52] (Fig. 7 (a)) and the L-shaped beam [48, 57, 58] (Fig. 7 (b)), each subjected to a concentrated force, are considered for compliance minimization and p-norm stress minimization

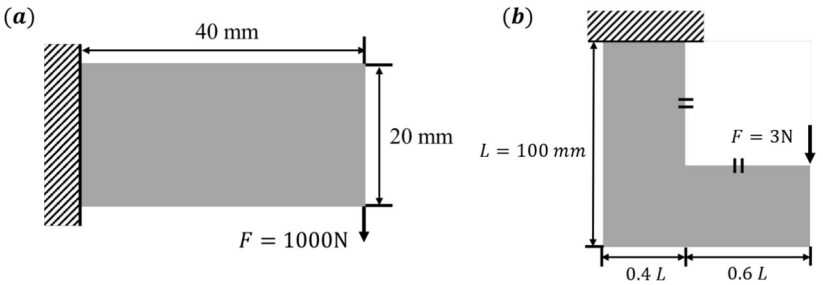

Fig. 7 **a** Problem domain of the cantilever beam used in compliance minimization, **b** Problem domain of the L-shaped beam used in stress minimization

problems, respectively. The force F is assumed to be small enough to ensure that the structure deformation is within the linear-elastic region. To avoid the singularity problem near the loading point, the force is equally distributed to the six material points located at the point [47]. Throughout the examples, uniform material properties are assumed, with Young's modulus set to 1×10^6 Pa and Poisson's ratio to 0.3. The target volume fraction (V^*) is set to 0.4. The penalization parameter pl, the stress penalization parameter q, and the p-norm aggregation factor p are set to 3.0, 0.5, and 12, respectively. The value for p was adopted based on several experiments, in alignment with findings from an earlier study [49]. In the subsequent examples, we utilized the globally convergent version of the Method of Moving Asymptotes (GCMMA) [59] with a movement limit of 0.3, alongside the density filter technique introduced by Bruns and Tortorelli [60], to achieve a binary design after iterative search.

5.1 Problems without the cell crossing error

This section presents the optimized layouts for compliance and stress minimization problems, accompanied by their convergence graphs to validate the proposed method. We further detail the optimized values and the iteration number at which convergence was achieved. These benchmark solutions align with the typical optimized layouts obtained using finite element analysis in topology optimization, due to the absence of cell crossing errors. It is important to note that although the objective values are comparatively lower than those reported in the literature [43], this discrepancy does not indicate the superiority or inferiority of our method compared to traditional topology optimization approaches using the finite element method.

5.1.1 Compliance minimization

Figure 8 shows the initial material point configuration and the corresponding von Mises stress field, analyzed using the MPM across different shape functions denoted as S_{vp}. As shown in Fig. 8, the background grid domain is larger than the structural boundary defined in Fig. 7 (a). A total of 3,200 material points are distributed within the structural boundary, as shown in Fig. 8 (a). Figure 8 (b) and (c) present two sets of results: one uses the standard MPM and the other employs the GIMP method. Remarkably, both sets of results exhibit identical displacement and stress, demonstrating that the outcomes are not affected by the choice of the shape function. In addition, the design sensitivities are also identical, as shown in the Appendix A. This finding leads to the conclusion that the continuity of the shape function does not affect the analysis as long as the cell crossing error is not present.

The iteration history of the layout, along with the number of iterations and the value of the objective function, is shown in Fig. 9 (a). The design, initially populated by gray elements (i.e., ρ between 0 and 1), evolves into a binary design during the optimization process. The evolution is typical of density-based methods, but is noteworthy in its efficiency and alignment with existing works. The corresponding volume fraction and the compliance convergence graph are plotted in Fig. 9 (b). The solution converged at the 76th iteration, where the objective value reached 83.57 and the volume constraint remained active. The resulting layout aligns with well-established material layouts, including those in literature [52, 61], which are conducted compliance minimization using FEA based SIMP method.

5.1.2 Stress minimization

Figure 10 presents the initial configuration of material points and their associated von Mises stress fields, meticulously analyzed through both the standard MPM and the GIMP method. The 6,400 material points is used to represent the L-beam. The expansive background grid, as detailed in Fig. 10 (a), is designed to ensure the material points are contained within the grid throughout the structural analysis. Both analysis models yield identical displacement, maximum stress and sensitivities (Appendix A), reconfirming the invariance of shape functions if the analysis is free from the cell crossing error as discussed in Sect. 5.1.1

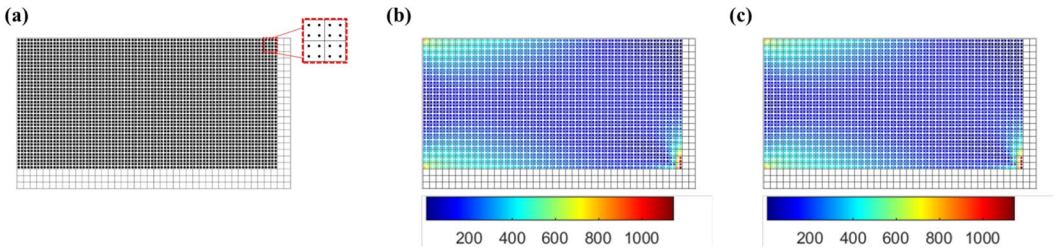

Fig. 8 **a** Material point distribution of the problem domain, structural analysis of von Mises stress field using **b** standard MPM and **c** GIMP method

Figure 11 displays the material layout changes and the convergence graph during the optimization, which are identical regardless of the shape function used. Both the p-norm stress and the material layouts during convergence are shown in Fig. 11 (a). Consistent with the other studies on stress minimization [11, 47, 49], optimized designs strategically avoid placing material at the internal corner where maximum stress occurs, as illustrated in Figs. 10 (b) and (c). As a result, p-norm stress is decreased by 97% after topology optimization. The convergence process is almost monotonic as depicted in Fig. 11(b). However, the final step of the iteration is found to be higher than the one in the compliance minimization problem discussed in Section 5.1.1 due to minor layout changes, as clearly demonstrated by the similarity between layouts from the 201st iteration as shown in Fig. 11 (a) which leads to violation of the convergence tolerance.

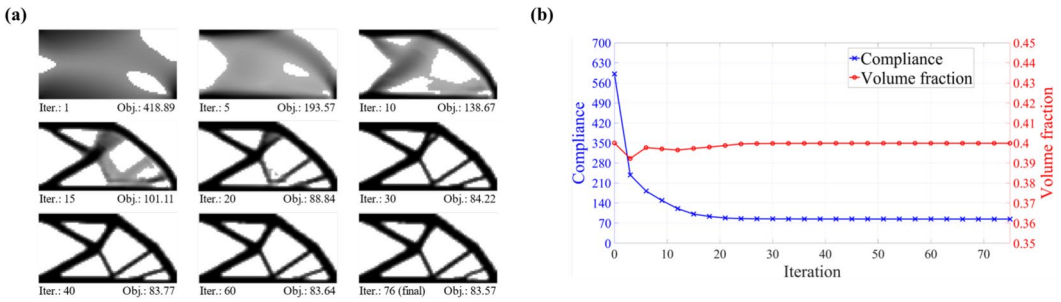

Fig. 9 Iteration history of **a** layout and **b** volume fraction and compliance in a cantilever beam with a concentrated force using standard MPM and GIMP method under the absence of the cell crossing error

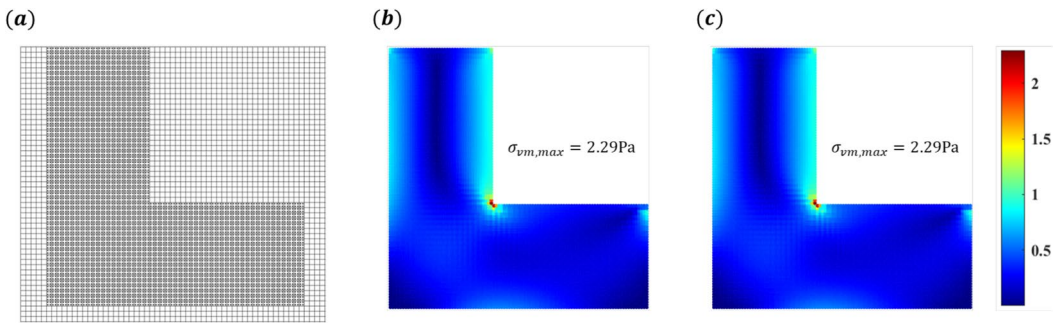

Fig. 10 **a** Material point distribution of the problem domain, structural analysis of von Mises stress field using **b** standard MPM and **c** GIMP method

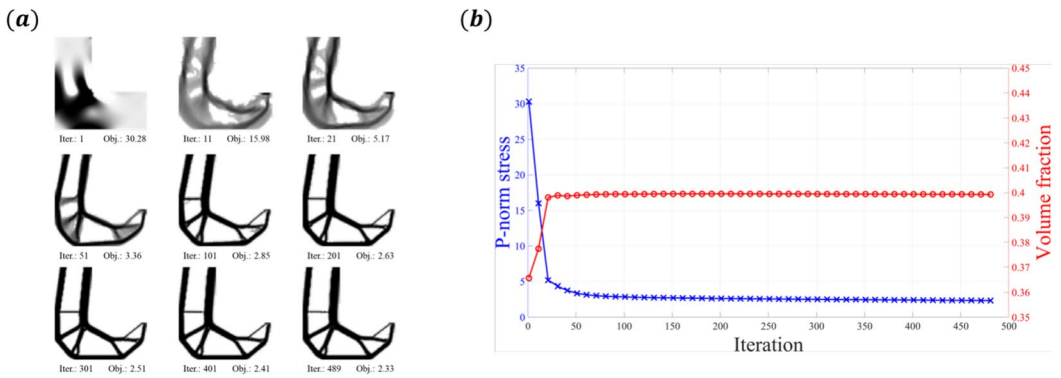

Fig. 11 Iteration history of **a** layout and **b** volume fraction and p-norm stress in a L-shaped beam using standard MPM and GIMP method under the absence of the cell crossing error

5.2 Effect of the cell crossing error

This section elucidates the effect of cell crossing errors — a well-recognized problem in MPM — on optimization results and convergence. The analysis employs the same benchmark problems of compliance and stress minimization discussed in Sect. 5.1. Cell crossing error arises when material points traverse cell boundaries, which causes discontinuities in the shape function gradient. However, cell crossing error does not necessarily occur in every instance where material points across multiple cells. To analyze its effect on topology optimization, we have intentionally induced cell crossing errors by shifting material points beyond the boundaries of background grid cells. For consistency with previous examples and to focus on the effects of cell crossing error under small deformation, the material points were deliberately shifted in the x direction.

5.2.1 Compliance minimization

The effect of cell crossing error is first examined in the compliance minimization problem, using the configuration described in Sect. 5.1.1. Initially, the impact of cell crossing error is particularly evident in the stress continuity, as illustrated in Fig. 12. The von Mises stress field shows periodic overshoots in the x direction when shifted particles near the cell boundaries crossed during the deformation, as shown in Fig. 12 (a). This fictitious discontinuity is mitigated by using the smoother shape function provided by the GIMP method, as shown in Fig. 12 (b). In addition, while the stress discontinuity is a noticeable effect, the accuracy of the displacement measurements is also affected by the induced error. Specifically, the tip displacement is significantly overestimated by 13.8% in the standard MPM analysis. However, this overestimation is reduced to less than 1.8% when using the GIMP method.

Figure 13 displays the optimized designs and optimization history obtained using the standard MPM and the GIMP methods. Cell crossing errors significantly impact the design layouts, as illustrated in the optimized layouts (Figs. 13 (a) and (b)). Compared to the layout using the GIMP method (Fig. 13 (b)), which aligns with designs without cell crossing errors, the layout from the standard MPM (Fig. 13 (a)) shows fictitious materials aligned along the y-axis, corresponding to the regions where material points crossed cell boundaries. These undesirable struts cause the objective function to converge at a higher value (90.99) compared to that of the GIMP (86.5), with increases of 9.6% and 3.7% over the case without errors, respectively. This phenomenon stems from an overestimation of sensitivities, influenced by the overestimated displacement gradient accountable by stress jumps (Fig. 12 (a)). However, it is important to note that this loss of optimality does not lead to inconsistency in the sensitivities; as shown in the convergence histories of both

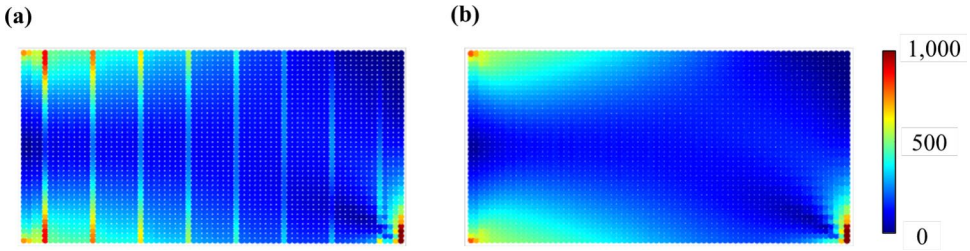

Fig. 12 von Mises stress fields of the cantilever beam model with material points with a small displacement; stress fields obtained using **a** the standard MPM and **b** the GIMP method

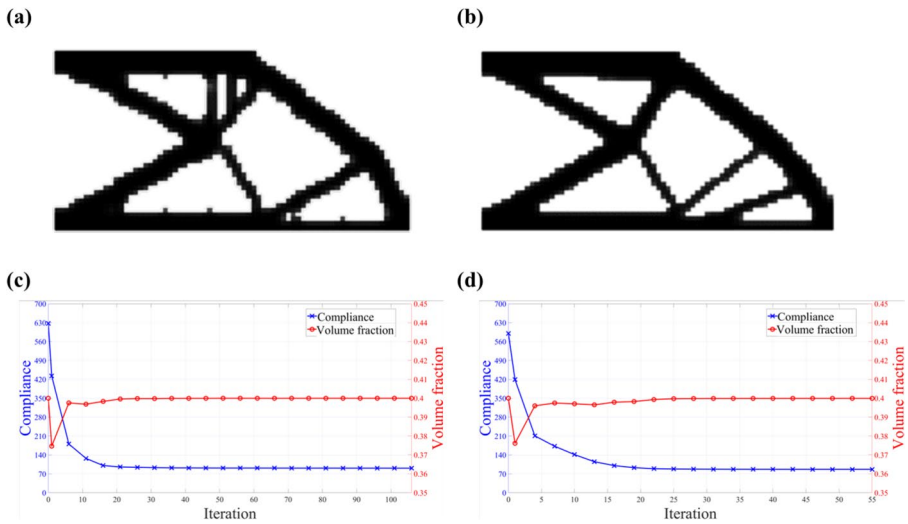

Fig. 13 Optimized layout for compliance minimization in the presence of a cell crossing error using **a** the standard MPM and **b** GIMP method; iteration history of compliance and volume fraction in compliance minimization using **c** the standard MPM (Obj: 90.99) and **d** GIMP method (Obj: 86.5)

methods (Figs. 13 (c) and (d)), the optimization processes exhibit similar monotonic convergence without noticeable oscillations.

5.2.2 Stress minimization

In this example, stress minimization is initially investigated in the presence of cell crossing errors using the standard MPM and GIMP method. Note that the impact of cell crossing errors is greater in MPM because the shape function is more involved in calculating stress than in compliance. The von Mises stress fields of the initial design are obtained by analysis using the FEM, standard MPM, and GIMP method (Figs. 14 (b) – (d)). All the results reveal a high concentration of stress at the re-entrant corner, but the stress distributions differ remarkably depending on the degree of mitigation of the cell crossing error. Specifically, Fig. 14 (c) shows a low measurement of von Mises stress, which appears as a line, deviating from the typical analysis as shown in Figs. 14 (b) and (d).

For a more intuitive comparison, the distribution of the von Mises stress along $\Gamma(\boldsymbol{\xi})$ in Fig. 14 (a) is shown among the FEM, standard MPM, and GIMP method. The comparison graphs are shown in Fig. 14 (e). The analysis based on the standard MPM shape function contains an oscillatory deviation in the stress; this deviation is induced by the cell crossing error, causing an overestimation of the p-norm stress by approximately 10%. In contrast, the results obtained using the GIMP method showed only a marginal difference compared to the FEM results.

Figure 15 shows the optimized layout, the corresponding von Mises stress field, and optimization history obtained using the standard MPM and the GIMP methods. Notably, Figs. 15 (a) and 15 (b) reveal that the optimized layout using the standard MPM method exhibits stress oscillations, with the maximum von Mises stress reducing from an initial 2.48 Pa to 1.81 Pa. In contrast, the optimized layout of the GIMP method significantly reduces the maximum von Mises stress from 2.24 Pa to 1.62 Pa, as shown in Figs. 15 (c) and 15 (d). Despite both methods demonstrating smooth convergence to optimal values in their respective iteration histories (Figs. 15 (e) and 15 (f)), the final optimized layouts differed markedly. This difference underscores the substantial impact that the choice of shape function has on the optimization result, particularly in mitigating the effects of cell crossing errors.

The objective and corresponding maximum von Mises stress values were higher in the design obtained with the standard MPM because of the reduced crispness of resolution in its optimized layout. The layout obtained using the standard MPM had poor crispness, in contrast to the result obtained using the GIMP function, which has a smooth boundary. This observation aligns with the results of compliance minimization, where the superior performance of the GIMP method is evident. Both outcomes stem from the overestimation of stress induced by cell crossing errors near the edges of the background grid. Consequently, the impact of cell crossing errors on stress optimization is more pronounced than on compliance optimization, highlighting the critical role of accurate stress estimation in achieving optimal designs.

6 Applications to configurable design spaces

Thanks to the design parameterization utilizing the density and position of the material points, the design space of the proposed method is highly reconfigurable from two

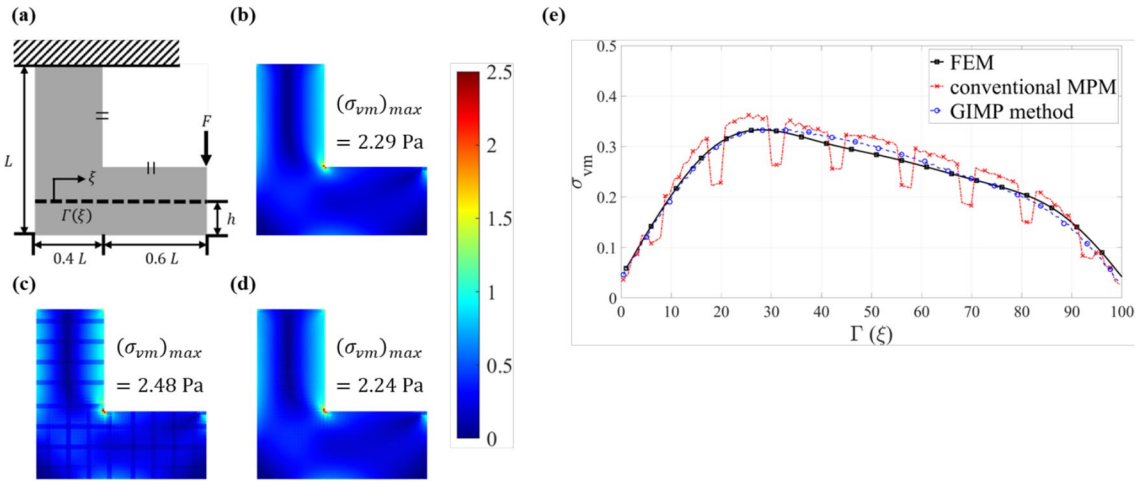

Fig. 14 **a** Problem domain of the L-shaped beam and von Mises stress field of this beam obtained with **b** the FEM, **c** standard MPM, and **d** GIMP method; **e** von Mises stress along the path of each method (the FEM, standard MPM, and GIMP method)

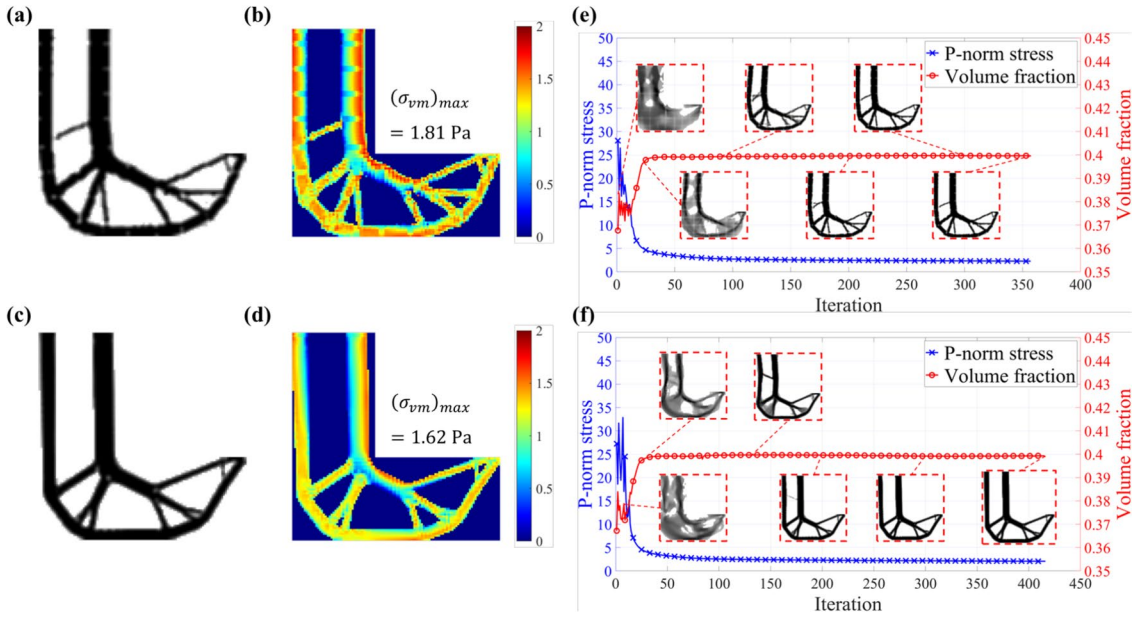

Fig. 15 Results of stress minimization: **a** optimized layout and **b** von Mises stress field of the optimized layout using the standard MPM; **c** optimized layout and **d** von Mises stress field of the optimized layout using the GIMP method, and iteration history of p-norm stress and volume fraction using **e** the standard MPM and **f** GIMP method

perspectives in compliance minimization. First, even with a coarse background grid, curved design spaces can be readily created by simply adjusting the density of material points, effectively altering the design domain. This approach differs from simply setting the density of the material point to zero, as it allows material to be reintroduced into the region without constraints. Secondly, the resolution of the design is easily adjustable by increasing the number of material points within each cell, thus facilitating multi-resolution topology optimization. Although multi-resolution topology optimization is not a novel concept, it is worth noting that the presented work simplifies this process by eliminating the need for complex numerical treatments beyond adjusting the span of the shape function, thus enhancing straightforwardness and efficiency.

6.1 Design domain specification

Figure 16 (a) illustrates the problem domain of the cantilever beam, which features a circular hole with a radius of 10 mm and a center located 15 mm from either end ($a = b = 15$ mm). The hole was created by removing material points within the specified void area, although the boundary of the hole does not align with the background grid. This removal process is crucial to differentiate from simply assigning a zero density to a material point, as discussed in Sect. 3.2.

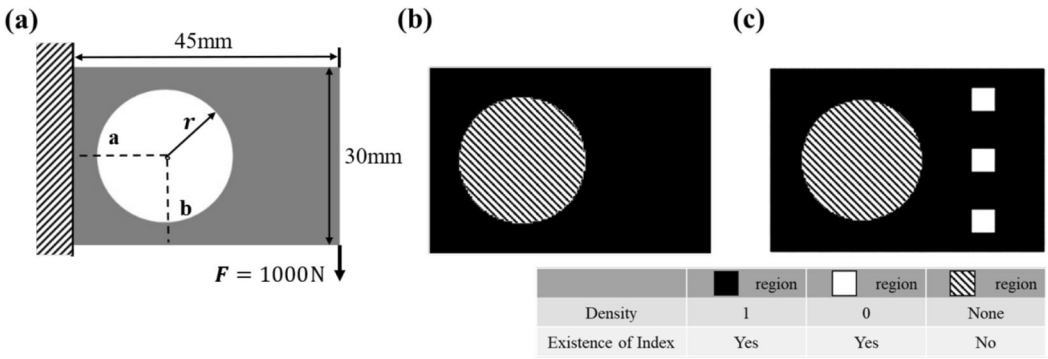

Fig. 16 **a** Problem domain of cantilever beam with a hole: **b** case 1: material point distribution of the problem domain with material points with a density of 1 and **c** case 2: material point distribution of the problem domain with densities 0 and 1 of the material points

A comparative analysis was conducted to highlight the differences between two cases in topology optimization. Figure 16 (b) shows the problem domain divided into two regions: the filled region, where the density is set to one and material points are present, and a shaded region, where there are no material points or density. In contrast, Fig. 16 (c) introduces white square regions, indicating areas where the density of the material points is zero.

The target volume fraction was set to 0.4 in both cases. Figure 17 shows the iteration history of the layout, along with the corresponding volume fraction and the compliance convergence graph. The optimized layouts were similar to those obtained using FEM, as earlier reported by Sigmund [52]. The optimality of both cases was comparable, with only a 1.4% difference in the objective value. It is important to note the distinct differences between the white and shaded regions in topology optimization. As shown in Figs. 17 (a) and (b), material points cannot be reintroduced into white regions during the topology optimization process, unlike in shaded regions where the density of the material points can be adjusted. This leads to a slower rate of convergence observed in case 2 compared to case 1.

This result demonstrates the difference between zero density material and the removal of material points. The former has limited influence on the design layout,whereas the latter can significantly alter the design domain without modifying the background mesh. This highlights the capability to easily implement complex changes in the design domain, which is particularly advantageous for coarse meshes.

6.2 Multi-resolution topology optimization

One advantage of MPM is the ability to freely add or remove material points without being constrained by the background grid. Since each material point has its own design space, controlling the resolution of the space becomes straightforward. Specifically, material points with different lengths of the material point domain l_p in Eq. (7), which relates to shape functions, permit variations in the distribution of material points within the design area. The proposed method inherently separates the analysis grid from the design grid, enabling multi-resolution topology optimization through the flexibility of the design variable. This method allows for an efficient exploration of the design space by considering both global and local features.

Figure 18 (a) displays a cantilever beam subjected to a distributed force on its top plate, a common example for multi-resolution topology optimization [10, 62, 63]. Three distinct cases are shown in Figs. 18 (b) - (d), all using the same background grid. The low-resolution example (Fig. 18 (b)) includes 9 material points per grid cell ($mp = 3$), totaling 4,050 points. Meanwhile, the high-resolution case (Fig. 18 (c)) consists of 36 material points per grid cell ($mp = 6$), amassing a total of 16,200 points. The multi-resolution case (Fig. 18 (d)) features 8,100 high-resolution points in the upper half and 2,070 low-resolution points in the lower half.

Compliance minimization is performed with the volume constraint set to 0.4. Figure 19 illustrates the optimized layouts in the three cases, along with their respective compliance values. In contrast to the low-resolution case (Fig. 19 (a)), the high-resolution example (Fig. 19 (b)) incorporates thin struts in the top-right corner, significantly reducing compliance. This result aligns with the findings reported by Groen et al. [62]. Figure 19 (c) presents the result of the multi-resolution topology optimization, closely resembling the high-resolution optimization layout. Typically, in multi-resolution topology optimization, the objective value tends to decrease roughly linearly as the number of design variables increases [64], allowing strategic allocation of material points to areas requiring detailed resolution while minimizing computational costs elsewhere. This approach results in designs that are both lightweight and structurally efficient, due to the inherent flexibility of the method, which permits precise control over the number and arrangement of material points and parameterization of the design domain.

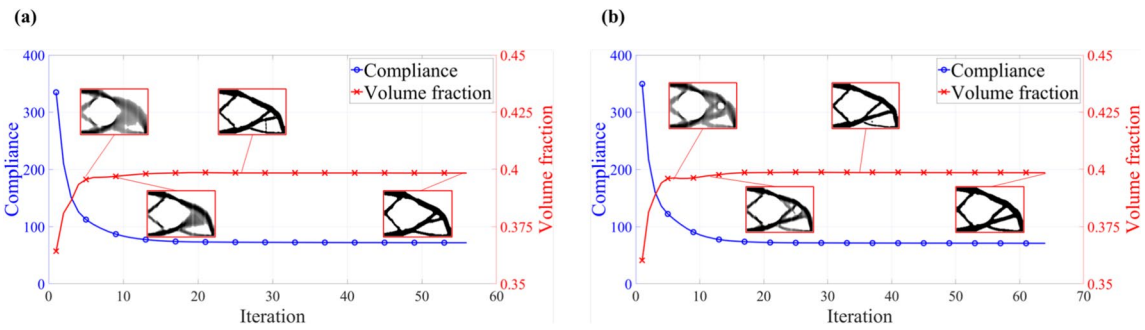

Fig. 17 Iteration history of compliance and volume fraction in the compliance minimization of **a** case 1 and **b** case 2

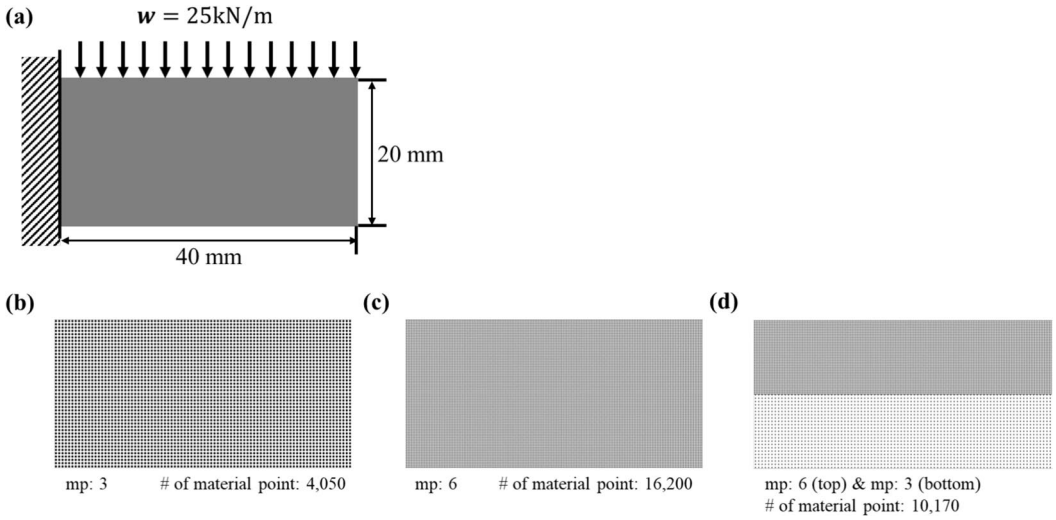

Fig. 18 **a** Problem domain of the cantilever beam with distributed force and the corresponding material point distributions with different numbers of material points: **b** 4,050 (low resolution), **c** 16,200 (high resolution), and **d** 10,170 material points (multi-resolution)

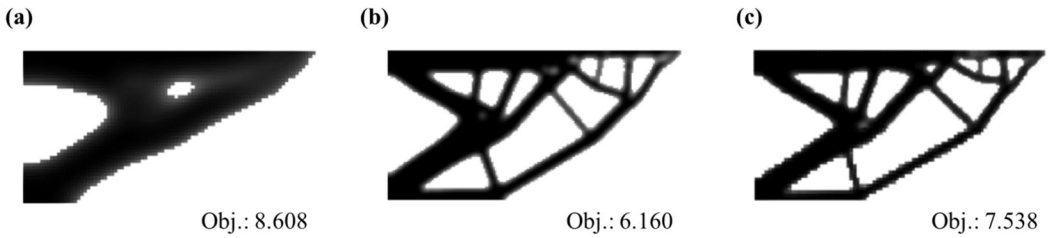

Fig. 19 Optimized layout obtained using different distributions of material points: **a** 4,050 material points (uniformly distributed), **b**: 16,200 material points (uniformly distributed), and **c**: 10,170 material points (non-uniformly distributed)

7 Conclusion

This study introduces a novel topology optimization method that leverages the capabilities of MPM analysis. This approach treats the density of the material points as design variables, correlating them with their initial position and volume. By presenting analytic sensitivities and leveraging the intrinsic variable mapping between background grids and material points inherent to MPM, our method achieves seamless integration into existing density-based frameworks, such as the SIMP method. This work rigorously validates these analytic sensitivities to ensure the robustness of our approach. For the first time, this study investigates the impact of cell crossing errors, which lead to fictitious stress discontinuities, and we demonstrate how the smoothness of shape functions influences solution optimality in such circumstances.

A significant advantage of our approach is the reconfigurability of the design domain, which permits the repositioning or addition of material points without necessitating modifications to the background grid or increasing the computational cost. Our numerical investigations clarify that the primary goal of this work is not to contest the optimality of current density-based methods but rather to explore the integration opportunities and address the challenges of incorporating MPM within existing topology optimization frameworks.

Given the capability of MPM to mitigate mesh-related issues such as mesh distortion and to adeptly handle complex scenarios like contact and detachment during extreme events (e.g., penetration), this method has significant potential to advance the field of topology optimization. In particular, we plan to explore a topology optimization framework that leverages MPM in conjunction with automatic differentiation (AD), aiming to enhance computational efficiency in sensitivity calculation under highly nonlinear problems. It opens new avenues for research and application, suggesting several promising directions for future exploration.

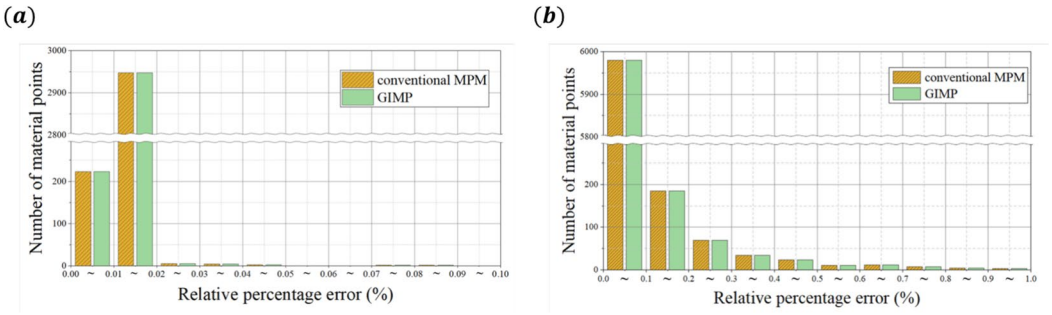

Fig. 20 Histogram of relative percentage error between numerical sensitivity and analytical sensitivity using standard MPM and GIMP method with different objective functions: **a** compliance and **b** p-norm stress

Appendix: Sensitivity verification

As outlined in Sect. 4, the sensitivity analysis is conducted under the assumption that the numerical inaccuracies induced during the mapping of material points to the background grid are negligible. This appendix compares the analytical sensitivities with those obtained by numerical differentiation to verify the accuracy of the sensitivity calculations. Both the cantilever beam and the L-shaped beam configurations are examined under conditions where cell crossing errors are not induced. This is because such errors do not impact the discrepancy between these sensitivities, provided that the analysis model and shape functions are consistently applied. The numerical sensitivities are derived using the forward finite difference method with a perturbation value ϵ of 10^{-4} as delineated in Eq. (A.1). This method is formalized as follows:

$$\left[\frac{dJ(\boldsymbol{\rho})}{d\boldsymbol{\rho}}\right]_{\text{num}} = \frac{J(\boldsymbol{\rho}+\epsilon)-J(\boldsymbol{\rho})}{\boldsymbol{\rho}}. \tag{A.1}$$

To confirm the validity of the calculated analytical sensitivity, the difference between the numerical and analytical sensitivity was assessed using the relative percentage error. The relative percentage error used here is calculated as

$$e(\%) = \left| \frac{\left[\frac{df(\boldsymbol{\rho})}{d\boldsymbol{\rho}}\right]_{num} - \frac{df(\boldsymbol{\rho})}{d\boldsymbol{\rho}}}{\frac{df(\boldsymbol{\rho})}{d\boldsymbol{\rho}}} \right| \times 100. \tag{A.2}$$

This study employs two different shape functions to investigate their impact on sensitivity analysis. Specifically, for each case, we investigate the compliance and p-norm stress sensitivities.

A total of 3200 material points were utilized to minimize compliance. Figure 20 (a) illustrates the compliance sensitivities in the absence of cell crossing errors using two distinct shape functions: standard MPM and GIMP. The analysis results demonstrate that both the standard MPM and the GIMP method exhibit comparable accuracy, with 99.15% of the design variables showing a relative percentage error of less than 0.02% in terms of compliance sensitivity.

Conversely, a total of 6400 material points were employed for p-norm stress minimization. Figure 20 (b) displays the p-norm stress sensitivities, again in the absence of cell crossing errors, using the same two shape functions. In scenarios without cell crossing errors, the sensitivity results derived from the two shape functions are found to be identical. In both compliance and p-norm stress cases, 98.97% of the design variables exhibited a relative percentage error of 0.3% for p-norm stress sensitivity. The errors in the results are relatively minor, with the stress sensitivity error being slightly lower than the compliance sensitivity error. This difference arises because the stress calculation is dependent on the gradient of the shape function, as outlined by Eq. (4).

Acknowledgements This work was supported by the National R&D Program through the National Research Foundation of Korea (NRF), funded by the Ministry of Science and ICT (No. NRF-2020R1C1C1005741, No. RS-2023-00257666), and the Human Resources Development of the Korea Institute of Energy Technology Evaluation and Planning grant funded by the Korea government Ministry of Trade, Industry and Energy (No. RS-2023-00240918).

Funding Open Access funding enabled and organized by Ulsan National Institute of Science and Technology (UNIST).

Data availability No datasets were generated or analysed during the current study.

Declarations

Conflict of interest The authors declare that they have no financial interests or personal relationships that could have influenced the work reported in this paper.

References

1. Zhu JH, Zhang WH, Xia L (2016) Topology optimization in aircraft and aerospace structures design. Arch Comput Methods Eng 23:595–622. https://doi.org/10.1007/s11831-015-9151-2
2. Yang RJ, Chahande AI (1995) Automotive applications of topology optimization. Struct Opt 9:245–249. https://doi.org/10.1007/BF01743977
3. Belytschko T, Liu WK, Moran B, Elkhodary K (2014) Nonlinear finite elements for continua and structures. John wiley & sons
4. Lee N-S, Bathe K-J (1993) Effects of element distortions on the performance of isoparametric elements. Int J Numer Methods Eng 36:3553–3576. https://doi.org/10.1002/nme.1620362009
5. Cervera M, Chiumenti M, Codina R (2011) Mesh objective modeling of cracks using continuous linear strain and displacement interpolations. Int J Numer Methods Eng 87:962–987. https://doi.org/10.1002/nme.3148
6. Mishnaevsky L, Lippmann N, Schmauder S (2003) Computational modeling of crack propagation in real microstructures of steels and virtual testing of artificially designed materials. Int J Fract 120:581–600. https://doi.org/10.1023/A:1025524214322
7. Jeong S, Lim S, Min S (2016) Level-set-based topology optimization using remeshing techniques for magnetic actuator design. IEEE Trans Magnet 52:1–4. https://doi.org/10.1109/TMAG.2015.2485260
8. Nguyen TH, Paulino GH, Song J, Le CH (2010) A computational paradigm for multiresolution topology optimization (mtop). Struct Multidiscipl Opt 41:525–539. https://doi.org/10.1007/s00158-009-0443-8
9. Kim YY, Yoon GH (2000) Multi-resolution multi-scale topology optimization - a new paradigm. Int J Solids Struct 37:5529–5559. https://doi.org/10.1016/S0020-7683(99)00251-6
10. Gupta DK, van Keulen F, Langelaar M (2020) Design and analysis adaptivity in multiresolution topology optimization. Int J Numer Methods Eng 121:450–476. https://doi.org/10.1002/nme.6217
11. Neofytou A, Picelli R, Huang T-H, Chen J-S, Kim HA (2020) Level set topology optimization for design-dependent pressure loads using the reproducing kernel particle method. Struct Multidiscipl Opt 61:1805–1820. https://doi.org/10.1007/s00158-020-02549-9
12. Wang Y, Lu E, Zhao J, Guo J (2015) Meshfree method for the topological design of microstructural composites. Comput Model Eng Sci 109–110:35–53. https://doi.org/10.3970/cmes.2015.109.035
13. O'Shaughnessy C, Masoero E, Gosling PD (2022) Topology optimization using the discrete element method. part 1: Methodology, validation, and geometric nonlinearity. Meccanica 57:1213–1231. https://doi.org/10.1007/s11012-022-01493-w
14. Masoero E, O'Shaughnessy C, Gosling PD, Chiaia BM (2022) Topology optimization using the discrete element method. part 2: Material nonlinearity. Meccanica 57:1233–1250. https://doi.org/10.1007/s11012-022-01492-x
15. Shobeiri V (2015) The topology optimization design for cracked structures. Eng Anal Boundary Elements 58:26–38. https://doi.org/10.1016/j.enganabound.2015.03.002
16. Zheng J, Yang X, Long S (2015) Topology optimization with geometrically non-linear based on the element free galerkin method. Int J Mech Mater Design 11:231–241. https://doi.org/10.1007/s10999-014-9257-y
17. Hur J, Kang P, Youn SK (2017) Topology optimization based on spline-based meshfree method using topological derivatives. J Mech Sci Technol 31:2423–2431. https://doi.org/10.1007/s12206-017-0440-6
18. Shobeiri V (2016) Topology optimization using bi-directional evolutionary structural optimization based on the element-free galerkin method. Eng Opt 48:380–396. https://doi.org/10.1080/0305215X.2015.1012076
19. Gonçalves DC, Lopes JDF, Campilho RDSG, Belinha J (2022) The radial point interpolation method combined with a bi-directional structural topology optimization algorithm. Eng Comput 38:5137–5151. https://doi.org/10.1007/s00366-021-01556-8
20. Garg S, Pant M (2018) Meshfree methods: A comprehensive review of applications. Int J Comput Methods 15:1830001. https://doi.org/10.1142/S0219876218300015
21. Krongauz Y, Belytschko T (1996) Enforcement of essential boundary conditions in meshless approximations using finite elements. Comput Methods Appl Mech Eng 131:133–145. https://doi.org/10.1016/0045-7825(95)00954-X
22. Sulsky D, Chen Z, Schreyer H (1994) A particle method for history-dependent materials. Comput Methods Appl Mech Eng 118:179–196. https://doi.org/10.1016/0045-7825(94)90112-0
23. Wieckowski Z (2004) The material point method in large strain engineering problems. Comput Methods Appl Mech Eng 193:4417–4438. https://doi.org/10.1016/j.cma.2004.01.035. ((**The Arbitrary Lagrangian-Eulerian Formulation**))
24. Lian Y, Zhang X, Liu Y (2011) Coupling of finite element method with material point method by local multi-mesh contact method. Comput Methods Appl Mech Eng 200:3482–3494. https://doi.org/10.1016/j.cma.2011.07.014
25. Jiang C, Schroeder C, Teran J, Stomakhin A, Selle A (2016) The material point method for simulating continuum materials, in: ACM SIGGRAPH 2016 Courses, SIGGRAPH '16, Association for Computing Machinery, New York, NY, USA, pp. 1–52. https://doi.org/10.1145/2897826.2927348
26. de Vaucorbeil A, Nguyen VP, Sinaie S, Wu JY (2020) Chapter two - material point method after 25 years: Theory, implementation, and applications, In: S. P. Bordas, D. S. Balint (Eds.), Advances in Applied Mechanics, volume 53, Elsevier, 185–398. https://doi.org/10.1016/bs.aams.2019.11.001
27. Stomakhin A, Schroeder C, Chai L, Teran J, Selle A (2013) A material point method for snow simulation. ACM Trans. Graph. doi 10(1145/2461912):2461948
28. Li Y, Li X, Li M, Zhu Y, Zhu B, Jiang C (2021) Lagrangian eulerian multidensity topology optimization with the material point method. Int J Numer Methods Eng 122:3400–3424. https://doi.org/10.1002/nme.6668
29. Liu H, Hu Y, Zhu B, Matusik W, Sifakis E (2018) Narrow-band topology optimization on a sparsely populated grid. ACM Trans Graph 37:1–14. https://doi.org/10.1145/3272127.3275012
30. Yuhn C, Sato Y, Kobayashi H, Kawamoto A, Nomura T (2023) 4d topology optimization: Integrated optimization of the structure and self-actuation of soft bodies for dynamic motions. Comput Methods Appl Mech Eng 414:116187. https://doi.org/10.1016/j.cma.2023.116187
31. Sato Y, Kobayashi H, Yuhn C, Kawamoto A, Nomura T, Kikuchi N (2023) Topology optimization of locomoting soft bodies using material point method. Struct Multidiscipl Opt 66:50. https://doi.org/10.1007/s00158-023-03502-2

32. Castillo E, Mínguez R, Castillo C (2008) Sensitivity analysis in optimization and reliability problems. Reliabil Eng Syst Safety 93:1788–1800. https://doi.org/10.1016/j.ress.2008.03.010. (**17th European Safety and Reliability Conference**)
33. Tan H, Nairn JA (2002) Hierarchical, adaptive, material point method for dynamic energy release rate calculations. Comput Methods Appl Mech Eng 191:2123–2137. https://doi.org/10.1016/S0045-7825(01)00377-2
34. Ma J, Lu H, Komanduri R (2006) Structured mesh refinement in generalized interpolation material point (gimp) method for simulation of dynamic problems. Cmes-Comput Model Eng & Sci 12:213–228
35. Homel MA, Brannon RM, Guilkey J (2016) Controlling the onset of numerical fracture in parallelized implementations of the material point method (mpm) with convective particle domain interpolation (cpdi) domain scaling. Int J Numer Methods Eng 107:31–48. https://doi.org/10.1002/nme.5151
36. Charlton T, Coombs W, Augarde C (2017) igimp: An implicit generalised interpolation material point method for large deformations. Comput Struct 190:108–125. https://doi.org/10.1016/j.compstruc.2017.05.004
37. Love E, Sulsky D (2006) An unconditionally stable, energy-momentum consistent implementation of the material-point method. Computer Methods in Applied Mechanics and Engineering 195:3903–3925. https://doi.org/10.1016/j.cma.2005.06.027
38. Guilkey JE, Weiss JA (2003) Implicit time integration for the material point method: Quantitative and algorithmic comparisons with the finite element method. Int J Numer Methods Eng 57:1323–1338. https://doi.org/10.1002/nme.729
39. Love E, Sulsky DL (2006) An energy-consistent material-point method for dynamic finite deformation plasticity. Int J Numer Methods Eng 65:1608–1638. https://doi.org/10.1002/nme.1512
40. Sulsky D, Kaul A (2004) Implicit dynamics in the material-point method. Comput Methods Appl Mech Eng 193:1137–1170. https://doi.org/10.1016/j.cma.2003.12.011. (**Meshfree Methods: Recent Advances and New Applications**)
41. Wang B, Vardon PJ, Hicks MA, Chen Z (2016) Development of an implicit material point method for geotechnical applications. Comput Geotech 71:159–167. https://doi.org/10.1016/j.compgeo.2015.08.008
42. Coombs WM, Charlton TJ, Cortis M, Augarde CE (2018) Overcoming volumetric locking in material point methods. Comput Methods Appl Mech Eng 333:1–21. https://doi.org/10.1016/j.cma.2018.01.010
43. Acosta JLG, Vardon PJ, Remmerswaal G, Hicks MA (2020) An investigation of stress inaccuracies and proposed solution in the material point method. Comput Mech 65:555–581. https://doi.org/10.1007/s00466-019-01783-3
44. Andersen S, Andersen L (2009) Analysis of stress updates in the material-point method. In: Damkilde L, Andersen L, Kristensen AS, Lund E (eds) The Nordic Seminar on Computational Mechanics. Aalborg University, DCE Technical Memorandum, Department of Civil Engineering, pp 129–134
45. Steffen M, Kirby RM, Berzins M (2008) Analysis and reduction of quadrature errors in the material point method (mpm). Int. J. Numer. Methods Eng. 76:922–948. https://doi.org/10.1002/nme.2360
46. Bardenhagen S, Kober E (2004) The generalized interpolation material point method. CMES - Comput. Model. Eng. Sci. 5:477–495. https://doi.org/10.3970/cmes.2004.005.477
47. Deng H, Vulimiri PS, To AC (2022) An efficient 146-line 3d sensitivity analysis code of stress-based topology optimization written in matlab. Opt. Eng. 23:1733–1757. https://doi.org/10.1007/s11081-021-09675-3
48. Le C, Norato J, Bruns T, Ha C, Tortorelli D (2010) Stress-based topology optimization for continua. Struct. Multidiscipl. Opt. 41:605–620. https://doi.org/10.1007/s00158-009-0440-y
49. Picelli R, Townsend S, Brampton C, Norato J, Kim H (2018) Stress-based shape and topology optimization with the level set method. Comput. Methods Appl. Mech. Eng. 329:1–23. https://doi.org/10.1016/j.cma.2017.09.001
50. Holmberg E, Torstenfelt B, Klarbring A (2013) Stress constrained topology optimization. Struct. Multidiscipl. Opt. 48:33–47. https://doi.org/10.1007/s00158-012-0880-7
51. Kočvara M, Stingl M (2012) Solving stress constrained problems in topology and material optimization. Struct. Multidiscipl. Opt. 46:1–15. https://doi.org/10.1007/s00158-012-0762-z
52. Sigmund O (2001) A 99-line topology optimization code written in matlab. Struct. Multidiscipl. Opt. 21:120–127. https://doi.org/10.1007/s001580050176
53. Sigmund O (2007) Morphology-based black and white filters for topology optimization. Struct. Multidiscipl. Opt. 33:401–424. https://doi.org/10.1007/s00158-006-0087-x
54. Langelaar M (2017) An additive manufacturing filter for topology optimization of print-ready designs. Struct. Multidiscipl. Opt. 55:871–883. https://doi.org/10.1007/s00158-016-1522-2
55. Liu K, Tovar A (2014) An efficient 3d topology optimization code written in matlab. Struct. Multidiscipl. Opt. 50:1175–1196. https://doi.org/10.1007/s00158-014-1107-x
56. Bendsøe MP (1989) Optimal shape design as a material distribution problem. Struct. Opt. 1:193–202. https://doi.org/10.1007/BF01650949
57. París J, Navarrina F, Colominas I, Casteleiro M (2009) Topology optimization of continuum structures with local and global stress constraints. Struct. Multidiscipl. Opt. 39:419–437. https://doi.org/10.1007/s00158-008-0336-2
58. Duysinx P, Bendsøe MP (1998) Topology optimization of continuum structures with local stress constraints. Int. J. Numer. Methods Eng. 43:1453–1478. https://doi.org/10.1002/(SICI)1097-0207(19981230)43:8<1453::AID-NME480>3.0.CO;2-2
59. Svanberg K (1987) The method of moving asymptotes-a new method for structural optimization. Int. J. Numer. Methods Eng. 24:359–373. https://doi.org/10.1002/nme.1620240207
60. Bruns TE, Tortorelli DA (2001) Topology optimization of nonlinear elastic structures and compliant mechanisms. Comput. Methods Appl. Mech. Eng. 190:3443–3459. https://doi.org/10.1016/S0045-7825(00)00278-4
61. Meisam Abdi IA, Wildman R (2018) Topology optimization of geometrically nonlinear structures using an evolutionary optimization method. Eng. Opt. 50:1850–1870. https://doi.org/10.1080/0305215X.2017.1418864
62. Groen JP, Langelaar M, Sigmund O, Ruess M (2017) Higher-order multi-resolution topology optimization using the finite cell method. Int. J. Numer. Methods Eng. 110:903–920. https://doi.org/10.1002/nme.5432
63. Gupta DK, Langelaar M, van Keulen F (2018) Qr-patterns: artefacts in multiresolution topology optimization. Struct. Multidiscipl. Opt. 58:1335–1350. https://doi.org/10.1007/s00158-018-2048-6
64. Sigmund O (2022) On benchmarking and good scientific practise in topology optimization. Struct. Multidiscipl. Opt. 65:315. https://doi.org/10.1007/s00158-022-03427-2